Applied Physics A manuscript No.
(will be inserted by the editor)

A ultra-wideband thin microwave absorber using inkjet-printed Frequency Selective Surfaces combining carbon nanotubes and magnetic nanoparticles

R. Jaiswar[1], F. Mederos-Henry[2], V. Dupont[3], S. Hermans[2], J.P. Raskin[1], I. Huynen[1]

Received: date / Accepted: date

Abstract A ultra-wideband microwave absorber (UWMA) combining Frequency-Selective-Surfaces (FSS) and dielectric layers is proposed. FSS patterns are printed by inkjet on dielectric layers using a resistive magnetic ink made of suspended carbon nanotubes decorated with Fe_3O_4 nanoparticles. The UWMA exhibits a huge fractional bandwidth of 140%, corresponding to reflectivity lower than - 10 dB and absorption higher than 90%, observed from 7 GHz to 43 GHz, meaning a 36 GHz bandwidth, for a thickness of only 0.26 λ. This performance is achieved through a proper selection of FSS surface resistance, tuned by the number of printed layers. Excellent agreement is observed between designed and measured low reflectivity and high absorption.

Keywords microwave absorber · carbon nanotube · magnetic nanoparticle · thin film · inkjet printing · metamaterial

1 Introduction

In the microwave band, extensive research has been conducted to develop metamaterial-inspired filters, polarizers, sensors, cloaking and electromagnetic shielding devices, microwave absorbers and so on [1,2]. In the last decade, metamaterial-based microwave absorbers have been widely studied due to their simplicity in planar design, ease of fabrication, low-cost and high-volume production [3]. In the past, classical Salisbury screens and similar structures were widely reported for microwave absorption, however their narrow bandwidth and large thickness have limited their applications [4,5]. In the recent past, researchers have proposed the circuital analysis approach for a Jaumann absorber where Frequency-Selective-Surfaces (FSS) are employed instead of the homogenous resistive sheets to facilitate the broadband absorption at lower thicknesses [6,7]. Many articles in literature reported as potential alternative changing the metallic FSS into low-conductivity or resistive printed FSS on dielectric substrate, so that the input impedance of the absorber can be modified not only by the geometry of the FSS but also through surface resistance (R_s) of the printed layer [8–12]. Printed electronics provides another set of advantages compared to the conventional lithography technology by facilitating low-cost mass production, ease-of-fabrication, reduced material waste and flexibility [13,14]. For conductive-ink materials used to print FFSs, there are some conventional metals available in the market such as silver (Ag), gold (Au), copper (Cu) [15,16]. Ag and Au are too expensive materials for making conductive ink developments so their use is limited, while Cu suffers from oxidation issues. On the other hand carbonaceous materials such as carbon nanotubes (CNTs) and graphene nanoplatelets (GNPs) possess excellent electrical and mechanical properties [17,18], as well as thermal and chemical stability, and high aspect ratio. Being also cost-effective, they are perfect candidates for conductive ink material [19,21,22]. Primary requirements of microwave absorbers are: wide operational bandwidth, low reflectivity (< - 10 dB), low thickness, along with ease-of-fabrication and low-cost mass-production.

[1] ICTEAM Institute, ELEN Division, 3 place du Levant, 1348 Louvain-la-Neuve, Belgium.
E-mail: rajkumar.jaiswar@uclouvain.be
[2] IMCN Institute, MOST Division, 1 place Lavoisier, 1348 Louvain-la-Neuve, Belgium.
[3] Belgian Ceramic Research Centre, 4 avenue Gouverneur Cornez, 7000, Mons, Belgium.

Mederos-Henry *et. al.* [23] reported various methods to modify the electrical properties of different carbonaceous materials by anchoring magnetic nanoparticles such as magnetite (Fe_3O_4) to fine-tune their electronic and magnetic characteristics and to be used in metamaterial-inspired applications. In this paper, we present experimental results of a thin ultra-wideband microwave absorber (UWMA) based on the inkjet printing of FSSs on a polycarbonate film supported on low-dielectric spacers. The required optimized surface impedance is obtained by using a water-based ink (CNT-ink) developed for inkjet printing. The CNT-ink is based on an aqueous dispersion (1% w/w) of multiwalled carbon nanotubes (MWCNTs) decorated with magnetite nanoparticles (MaNPs). Microwave shielding structures developed through the inkjet-technology have a promising future in the production of broadband thin, flexible, low-cost, and light-weight absorbing materials.

2 Materials and methods

2.1 Ink preparation

The synthesis of the MaNPs@MWCNTs is fully described in [23]. In a typical procedure, 250 mg of MWCNTs were dispersed into a mixture composed of 67 mL ethylene glycol (EG), 33 mL polyethylene glycol 400 (PEG-400) and 33 mL Milli-Q water. The suspension was sonicated for 2 hours. Afterwards, 1.18 g of iron (III) acetylacetonate ($Fe(acac)_3$) were added under magnetic stirring. Crushed NaOH pellets were added until the solution pH value was set to 12. The mixture was then transferred into a stainless steel autoclave vessel, heated up to 220°C (approx. 50 minutes) and maintained at that temperature for 15 hours while stirring at 500 rpm. In the described procedure:

- sonication was performed in a VWR ultrasound cleaner USC 1200-THD at 80 W sonication power;
- the autoclave temperature was automatically regulated by a Parr 4836 temperature controller (Parr Instrument Company, USA) having an average heating rate of 4°C/min;
- the autoclave inner atmosphere was not purged nor modified in any manner during the synthesis, while the system pressure was left to build up during heating without any type of external control;
- when the heating time was completed, the autoclave was immediately immersed in an ice bath and cooled down to ambient temperature;
- the obtained products were separated by magnetic decantation, filtered over a PVDF filter (Millipore GVWP02500, 0.22 μm pore size) and rinsed six times, alternating Milli-Q water and ethanol. Afterwards, they were dried under vacuum, at room temperature for 12 hours.

A simple sonication approach was employed to prepare the ink. Specifically, 1 g of nanopowder was dispersed in 100 g of distilled water. As the wettability of MWCNTs was very poor in distilled water, 1 g of Triton X100 powder was incorporated to decrease the surface tension of the distilled water and maintain the powder in suspension. It was followed by sonication carried out with a Bioblock Scientific Vibracell 75041 sonicator during 6 minutes (10 sec ON; 10 sec OFF). During this treatment, the solution cup was placed in a bath of iced water to prevent the temperature from rising and thus avoid evaporation of the aqueous solution. After this treatment, the solution became a gel, and another dispersant, 0.25 g of Disperbyk 190, was incorporated. The resulting solution was sonicated as described above, giving a very fluid suspension. Afterwards, the dispersion was centrifuged using a Heraeus Sepatech 2520 centrifuge to remove impurities and possible remaining powder aggregates which could clog the print heads nozzles. The centrifugation cycle of 30 minutes was performed at 2500 rpm and the supernatant was collected. After this treatment the suspension became very stable in time and very opaque without clarification.

2.2 Inkjet printing process

The inkjet printing was carried out by using a Fujifilm Dimatix Materials Printer (DMP-2800) equipped with a 10 pL drop cartridge (DMC-11610). The set of parameters of the ink droplet sequence for printing was tailored by adjusting the ejecting waveform (voltage and frequency of the piezoelectric crystal which controls the droplets ejection). The waveform parameters depend on the ink characteristics like surface tension and viscosity. In addition, to ensure the uniformity of the deposited MWCNTs film, the following parameters were kept constant: 25 μm drop spacing for a 35 μm drop size, while the printing area and the cartridge were used at room temperature. The substrate used for printing is a Polycarbonate sheet (Lexan 8B35E) from Sabic. According to the literature[28], annealing temperature and time have a significant influence on the electrical behavior of the printed patterns. Thus, these were placed in a drying oven at 85°C for 1 hour to achieve a stable and constant surface resistance.

2.3 Materials characterization

2.3.1 Transmission electron microscopy (TEM)

The as-synthetized MaNPs@MWCNTs nanocomposite powder was dispersed in hexane or ethanol by sonication. Three drops of the supernatant were then deposited onto a holey carbon film supported on a copper grid (C-flat, Protochips, USA), and left to dry, overnight, at room temperature under vacuum. TEM images were obtained on a LEO 922 OMEGA Energy Filter Transmission Electron Microscope operating at 120 kV.

2.3.2 X-ray powder diffraction (XRPD)

The as-synthetized MaNPs@MWCNTs nanocomposite powder was introduced into 0.5 mm thin-walled glass capillaries (Hilgenberg GmbH, Germany), mounted on a goniometer head and kept at 200 mm distance from the detector. Diffractograms were then collected at room temperature using a MAR345 diffractometer (Mar Research GmbH), a Mo-K (0.71073) anode and a XENOCS focusing mirror. The obtained 2D diffractograms were azimuthally integrated using the Fit2D software, calibrated with a LaB6 standard (NIST 660b Standard).

2.3.3 Thermogravimetric analysis (TGA)

A few milligrams (5-10 mg) of the CNT-ink were previously scrapped-off from the Lexan film with a clean scalpel. The recovered powder was placed in alumina containers and introduced in a Mettler Toledo TGA/ SDTA 851e instrument. Thermograms were recorded up to 900 °C using a 10 °C/min heating rate under an air flux. The samples were recovered after heating and analyzed by XRD as described above, identifying a hematite (Fe_2O_3) phase. TGA data treatment required for the calculation of the MaNPs massic loading rate was based on the formula weight of this particular iron oxide phase. Corrections for residual non-carbonaceous impurities present in MWCNTs were also included in these calculations.

2.4 Direct current (DC) surface resistance (R_s) characterization

Square patches printed using 3, 5, 8 and 10 layers of MWCNTs-ink were cut into five individual bands of equivalent dimensions. A conductive silver paste (G3790, Agar Scientific Ltd) was deposited at regular intervals to ensure good electrical contact with the meter probes. Each zone delimited by two silver paste electrodes was measured using a B2902A Agilent IV meter equipped with two probes. Resistance R measurements were performed in different points of each zone. The surface resistance $R_S(\Omega/sq.)$ was calculated from measured resistance R as:

$$R_S = \frac{R}{w\,l} = \frac{1}{\sigma\,t} \tag{1}$$

where w, l are width and length of the printed patches and σ, t are the conductivity and thickness of printed layers, respectively.

2.5 Microwave characterization

The fabricated FSS was measured using a waveguide method [26] in the C, X, Ku, Ka and U-band (5-50 GHz total frequency range) with an Agilent PNA-X vector network analyzer. TRL calibration was applied to measure the scattering parameters S_{11} and S_{21}, which were used to evaluate the reflectivity and absorption performances of the absorber. The measurement configuration is illustrated in Figure 1. The FSS absorber was sandwiched between waveguide ports connected to the vector network analyzer via coaxial cables. TRL calibration moves the reference planes for the characterization at input and output interfaces of the absorber.

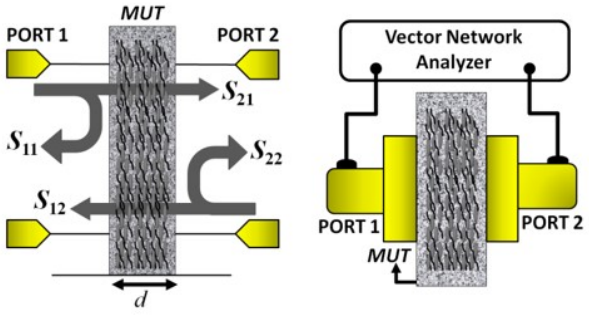

Fig. 1 Measurement configuration showing the Material Under Test, i.e. the FSS absorber, inserted between rectangular waveguide ports.

3 Results and discussion

3.1 Physico-chemical Characterization of the MaNPs @MWCNTs nanocomposite and ink

Figure 2 shows the TEM image of the as-obtained MaNPs @ MWCNTs nanocomposite powders while Figure 3 presents its X-Ray diffraction pattern. As it can be observed there, the recorded diffraction peaks are distinctive of magnetite (Fe_3O_4). Other closely associated magnetic phases such as maghemite (γ-Fe_2O_3), whose characteristic diffraction peaks are located between 2θ values of 6° and 12°, are not detected. As for the reflection observed around $2\theta = 12°$, it has been attributed to the ordered arrangement of the MWCNTs concentric cylinders of graphitic carbon [34]. The SQUID characterization data of similarly prepared Fe_xO_y/C powders has been reported elsewhere [23]. A magnetization saturation value of 60 emu/g was found, also reported in [29]. The thermogravimetric analysis (TGA) of the CNT-ink allowed determining that the dispersants, MWCNTs and MaNPs account for 53%, 25% and 22% of its mass, respectively.

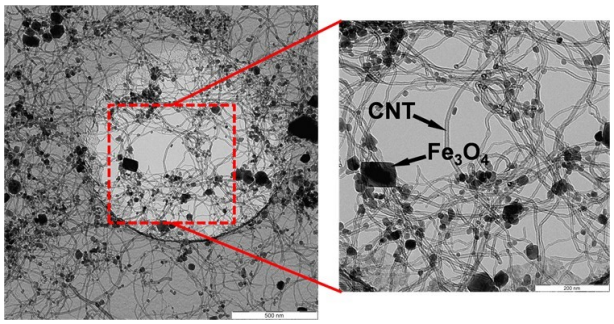

Fig. 2 TEM image of the MaNPs@MWCNTs nanocomposite.

3.2 Electrical characterization of the MaNPs@MWCNTs ink

Figure 4 presents the measured surface resistance, R_s, of 3, 5, 8 and 10 thermally-annealed layers printed on a polycarbonate sheet using the MaNPs@MWCNTs ink. As it can be seen, the measured surface resistance R_S shows an exponential decrease as the number of printed layers increases from 3 to 10. These results show that as the number of printed layers increases, so does the number of conductive paths available for electron transport

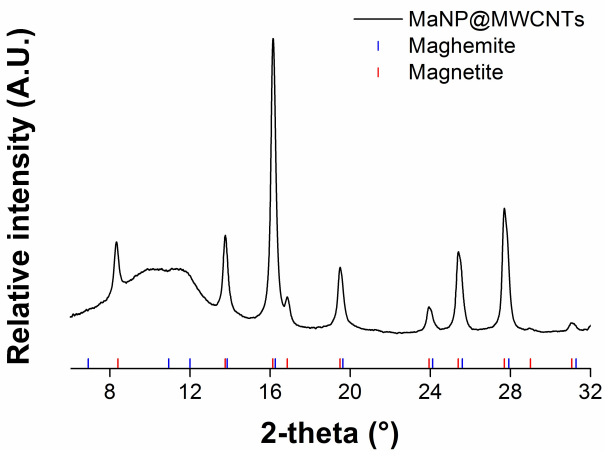

Fig. 3 XRD measurement of the MaNPs@MWCNTs nanocomposite. Blue: expected peaks for a maghemite phase, red: expected peaks for a magnetite phase

through the MWCNT network within the CNT ink, resulting in improved conductivity. Since MWCNTs have a flexible tubular shape, they can form an entangled interconnected network to support current transport. Due to practical limitations, a number of prints larger than 10 was not considered. Nonetheless, this number of layers was proven to be efficient for our intended application.

It is worth noticing that an interferometric profile of 5 CNT-ink layers was carried out to estimate the thickness of the CNTs film, which was found to be less than 50 μm.

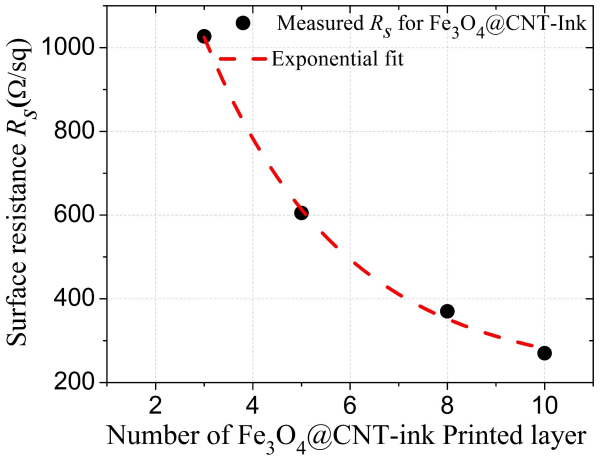

Fig. 4 Measured Surface resistance R_s for magnetic (Fe_3O_4)-CNT ink printed layers.

3.3 Microwave absorber

3.3.1 Design

In order to design a broadband absorber, various types of structures (e.g. cross-dipole, mesh-grid, Jerusalem-cross, square-ring, etc) were simulated using CST Microwave Studio, having different R_s values obtained from the results presented in Figure 4. The corresponding multilayers were analyzed for minimum reflectivity. Figure 5 represents the schematic structure of the chosen ultra-wideband microwave absorber (UWMA) and the unit cell simulated using the same software. Resistive FSSs having surface resistance of $R_{S1} = 600\ \Omega/sq$ (top) and $R_{S2} = 270\ \Omega/sq$ (bottom) laminated between two 125 μm thin polycarbonate (PC) films were first simulated alone for determining their resonant frequencies responsible for zero reflection. Then these two laminates were sandwiched between three low-dielectric substrate spacers (Rogers 5880, $\varepsilon = 2.2$) having thicknesses (d_1, d_2, d_3) and backed by a copper ground plane. The top designed FSS, having surface resistance R_{S1}, is a mesh-grid enclosing Jerusalem-cross (JC) while the bottom FSS (R_{S2}) consists of a mesh-grid enclosing a square-ring and a cross-dipole. These FSSs have been widely studied and are well known for their design flexibility and simplicity in fabrication, while their electromagnetic behavior can be varied to achieve the low reflection required frequencies. The whole structure was then simulated using the same software and optimized to achieve -10 dB reflectivity in a large frequency bandwidth between 5-50 GHz.

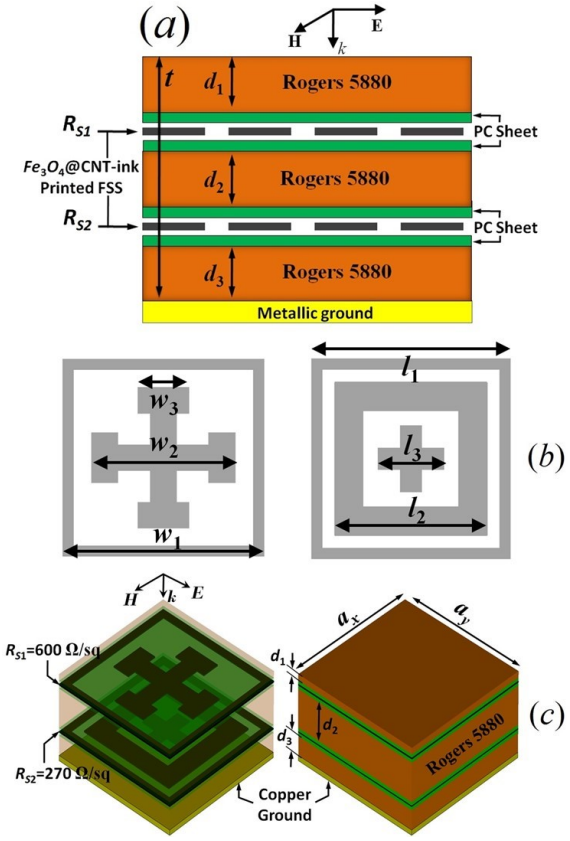

Fig. 5 Schematic structure of MaNPs@MWCNTs ink-based wideband absorber. a) Schematic structure of Ultra-wideband microwave absorber (UWMA), b) Resistive FSS for top and bottom CNT-inked layer of unit cell, c) Perspective view of constituent layers in the structure. Dimensions in the structure are: $a_x = a_y = 9.0$, $d_1 = 0.25$, $d_2 = 1.5$, $d_3 = 0.75$, $w_1 = 9$, $w_2 = 6.43$, $w_3 = 2.3$, $l_1 = 9$, $l_2 = 6.93$, $l_3 = 3.0$. Units are in mm.

The absorption mechanism is the combination of two phenomena. The basic structure is a Salisbury screen configuration, i.e. a dielectric substrate backed by a metallic plane and covered with a resistive film. At a specific frequency (i.e. when the corresponding wavelength is 4 times the thickness of the slab), the wave is able to enter the Salisbury structure without reflection, is trapped between the resistive sheet and the back plane where it is reflected, and undergoes attenuation due to the resistivity of the film. The presence of the backing plane allows to maximize the absorption by reflecting back the fraction of signal that was not absorbed when travelling through the two FFS layers, that becomes absorbed again when reflecting through the FSS. The shape, size and number of the FFS patterns are designed using CST simulation to modify the input impedance of the device, i.e. to achieve several zeros of reflection in the desired frequency range, favoring the penetration of the wave in the absorber, and then its absorption in a wide frequency range owing to the number of zero reflections. The design takes into account the predefined thickness of the selected Lexan dielectric spacers. These films were chosen for their reduced thickness (i.e. for better compacity) and low dielectric constant in order to minimize reflection of the incoming wave at the interface with air. Rogers dielectric substrates were selected following same requirements to maintain the printed Lexan films sandwiched and rigid. The wave incoming normal to the FSS surface interacts with the lossy patterns, being absorbed by them. The design method is detailed in [5]. The simulated absorption is illustrated in Figure 6, which shows the distribution of the field across the section of the absorber geometry at the two ends of the frequency band, i.e. at 9 and 40 GHz. As expected, the field is almost equal to zero after passing through the FSS structures.

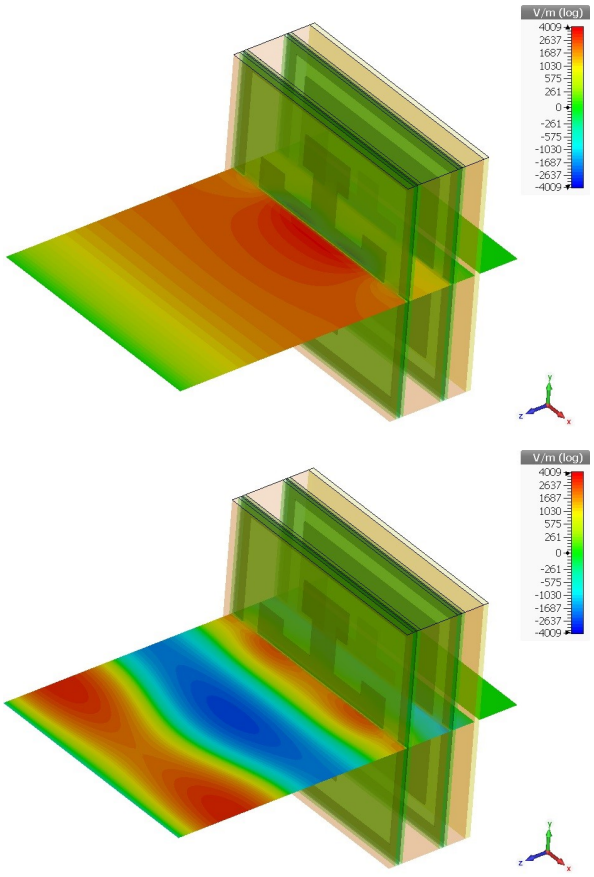

Fig. 6 CST simulation of electric field distribution in the structure depicted in Figure 5. Top : at 9 GHz, bottom: at 40 GHz. The wave is coming from the left and propagates towards the negative z-direction.

3.3.2 Experiments

For the experimental measurements, a sample of 100 x 100 mm was printed on a polycarbonate film as shown in Fig. 7 using the printing conditions described in section 2.2. It was then sandwiched between the Rogers 5880 dielectric spacers to fabricate the UWMA. Its scattering parameters S_{11} and S_{21} were measured as described in section 2.5.

Figure 8 and 9 present the reflectivity R and associated absorption A in the 5-50 GHz frequency range of the MaNPs@MWCNTs ink-based UWMA having a conducting backing plane. Reflectivity and absorption are obtained from the S-parameters as:

$$R = |S_{11} - \frac{{S_{21}}^2}{1 + S_{22}}| \quad (2)$$

$$A = 1 - R^2 \quad (3)$$

Measured and simulated results are in good agreement showing - 10 dB reflectivity and 90% absorption in the

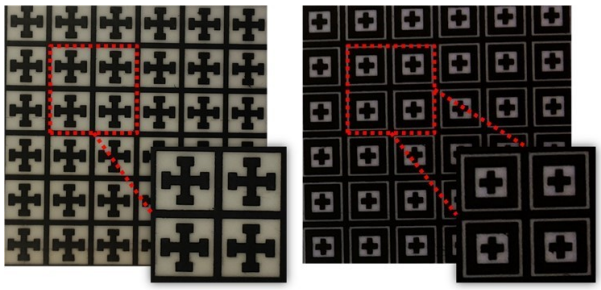

Fig. 7 Photograph of MaNPs@MWCNTs ink printed FSS on polycarbonate film for (left) Top FSS and (right) Bottom FSS (Inset: zoom on unit cell portion).

7-43 GHz band, meaning a 36 GHz bandwidth for an absorber thickness of 3 mm which corresponds to 0.26 λ. The obtained fractional bandwidth is huge: 140 % as demonstrated in Figure 9.

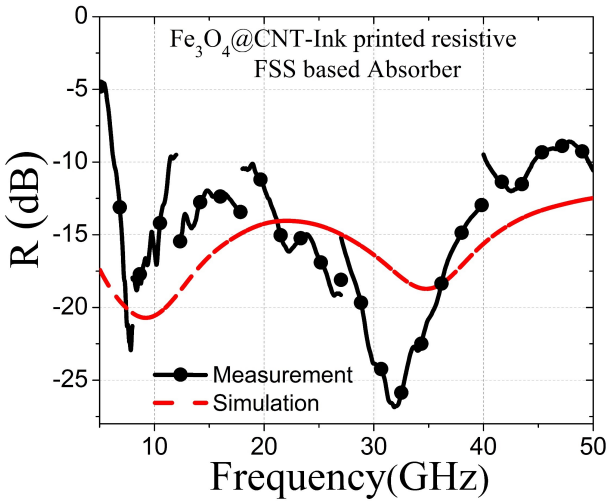

Fig. 8 Measured and simulated reflectivity R for the UWMA absorber based on FSSs printed using MaNPs@MWCNTs ink.

It is worth noticing that the jumps observed in the measured curves in Figures 8 and 9 are due to the measurement method used for reflection and absorption. The S-parameters are measured using a waveguide method described in section 2.5. In order to cover the whole bandwidth several waveguides of decreasing sections have to be used, corresponding to C, X, Ku, K, Ka, and U frequency band, respectively. Each jump corresponds to a change of band, hence of waveguide size.

3.3.3 Discussion

To conclude we compare our UWMA absorber with other structures recently published in the scientific lit-

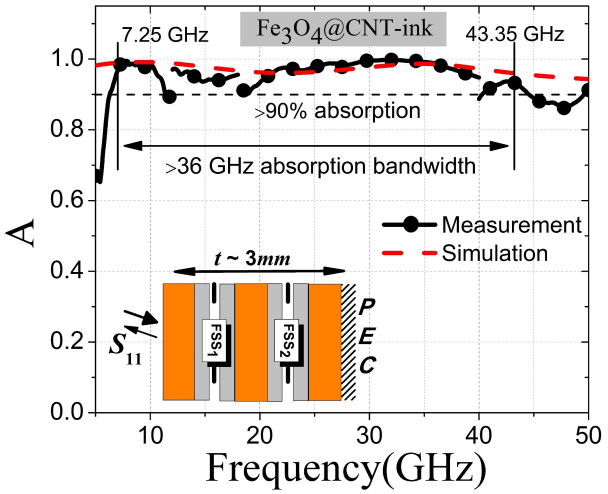

Fig. 9 Measured absorption A for the UWMA absorber based on MaNPs@MWCNTs ink-printed resistive FSSs. $A > 90\%$ in a > 36 GHz bandwidth.

erature. Their microwave absorbing performances are reported in Table 1.

In [29], hollow particles of Fe_3O_4 are combined with carbon nanotubes and dispersed into paraffin to measure the permittivity and magnetic permeability of the composite. The measured values are used to simulate the reflection loss (RL) of the composite using a Salisbury configuration in which the slab, having the parameters of the loaded paraffin, is backed by a metallic reflecting ground plane. Two thicknesses are considered: 1.5 mm and 2.0 mm. For 2 mm, the reflectivity R resulting from this Salisbury-type configuration is < -10 dB over a bandwidth not exceeding 4 GHz, from 12 to 16 GHz, while our structure achieves the same reflectivity from 7 to 40 GHz, for a thickness of 3.5 mm. While our thickness is higher, the huge bandwidth induces a Figure of Merit (FoM) superior to other works reported, as shown in Table 1. However no experimental validation of RL is provided in [29]. Magnetic hysteresis loops reported revealed saturation magnetization values ranging from 60 to 72 emu/g.

In [30] grapes of Fe_3O_4 nanoparticles are combined with carbon nanotubes and their measured permittivity and permeability are again used for simulating a Salisbury configuration. A reflectivity R < - 10 dB is observed between 7.5 and 11 GHz only, and for a thickness of 3.2 mm. Those performances are inferior to those of our work (see Table 1), as well as the reported saturation magnetization equal to roughly 50 emu/g.

In [31] a CNT@TiO_2 sponge is dispersed into paraffin, in order to measure the permittivity and permeability. Then, the reflectivity is simulated for a Salisbury configuration using various thicknesses. RL < - 10 dB is observed at low frequency over only 1.7 GHz bandwidth, from 6 to 7.7 GHz, for a 2 mm thickness. Such results are less performant than our work, as shown by the respective FoM in Table 1.

The work in [32] differs from our work in several ways. Firstly, the geometry and fabrication of the unit cell is 3D-machined and thus more complicated, compared to the 2-D fully planar and thin ink-printed FSS structure in our work. Secondly, absorption occurs in the bulky epoxy resin loaded with Fe particles, while in our work the absorption is induced by the thin FFS printed patterns. Also, even if the presented RL concept is fully equivalent to our definition of reflectivity R (3), it is narrowband (RL < -10 dB from 8 to 28 GHz), and its center frequency is highly dependent on the thickness of the absorber. In our work, the reflectivity R shows a wider bandwidth (R < -10 dB from 7 to 38 GHz), which is primary fixed by the FSSs topologies. Finally, the thickness of the absorber is 5.5 mm in [32], while our absorber is thinner, i.e. 3.5 mm, and induces again a higher FoM, as shown in Table 1.

The work in [33] presents a 3D geometry similar to [32], involving a 4-layer configuration. Its performance is similar to our work : both achieve RL lower than 10 dB from 8.5 to 40 GHz. However its thickness is 5 mm, thus higher than the value of our absorber, so that its FoM is again lower.

The data labeled CNT-ink correspond to an absorber having same FSS geometries as the present paper, but printed using a ink containing only CNT.

Ref.	f_o (GHz)	BW (GHz)	FBW (%)	d (mm)	FoM
[29]	13.9	4.2	30.2	2.0	389
[30]	9.00	3.5	38.9	3.2	503
[31]	6.85	17	24.3	3.0	414
[32]	19.0	20	105.3	5.5	638
[33]	24.3	31.5	130	5.0	917
CNT-ink	24.5	34	138	5.1	1078
present work	25.3	36	142	3.5	1671

Table 1 Performances of composite absorbers from literature, compared to our work. f_o is the center frequency, BW is the bandwidth of absorption, FBW is the fractional bandwidth defined as FBW = BW / f_o, and FoM is the Figure of Merit defined as FoM = FBW / d, and d is the global thickness of the absorber.

Two main conclusions can be drawn. Firstly, FFS-ink strucures outperform the other devices in term of FoM, resulting from both higher bandwidth and reduced thickness, since absorption occurs only at thin FFS interfaces rather than into bulky layers. As explained before in Section 3.3.1, the shape and number of FSS enable to tailor the low reflection bandwidth and resulting absorption, at fixed thin dielectric layers

thickness. Secondly, the addition of magnetic particles enables to modify the impedance condition at the FSS interfaces, so that resonances responsible for absorption can occur at lower thicknesses. As a consequence the overall thickness of the absorber can be significantly reduced, resulting into an optimal FoM value.

4 Conclusion

As a conclusion, the proposed MaNPs@MWCNTs ink-based UWMA combines compacity and ultra-wide band absorption through a proper choice of surface resistances, controlled by the number of printed layers. Also, the presence of magnetic inclusions increases the input impedance of UWMA, that becomes closer to air impedance. This explains the observed low reflectivity over such a wide band. We have opened a new avenue for absorbers based on FSSs printed with magnetic-CNT ink, that can be exploited for tunability effects under magnetic field or current control.

Acknowledgements The authors are grateful to the National Fund for Scientific Research (F.R.S.-FNRS, Belgium) for supporting this research. This work is also supported by the Walloon region, and by the "Communauté Française de Belgique", through the project "Nano4waves" funded by its research program "Actions de Recherche Concertées". Special thanks are also due to Mr. S. Depaifve and Profs. A. Delcorte and C. Bailly for fruitful discussions in the frame of the Nano4waves project.

References

1. C. Caloz, T. Itoh "Electromagnetic Metamaterials: Transmission Line Theory and Microwave Applications: The Engineering Approach", 2006 John Wiley and Sons, Inc..
2. R. Marques et al. , "Metamaterials with Negative Parameters: Theory, Design, and Microwave Applications", 2008 John Wiley and Sons, Inc.
3. C. Watts et al., Adv. Mat. **24**, 98120 (2012).
4. B. Chambers, IEE Electron. Lett., **30**, 1353 - 1354, (1994).
5. F. Che Seman et al., IET Microwaves, Antennas and Propagation **5**, 149 - 156 (2011).
6. A. Kazemzadeh and A. Karlsson, IEEE Trans. Antennas Propag., **58**, 3637 - 3646 (2010).
7. A. Kazemzadeh, IEEE Trans. Antennas Propag., **59**, 135 - 140 (2011).
8. E. Yildimy, O. Aydin Civi, Proc. of 5th Euro. Conf. on Antenna and Prog. (EUCAP), 2011.
9. M.Olszewska-Placha, IEEE Trans. Antennas Propag., **63**, 565 - 572 (2015).
10. F. Costa et al., IEEE Trans. Antennas Propag., **58**, 1551 - 1158 (2010).
11. X. Huang et al., Sci. Reports, **6**, 38197 (2016).
12. W.J. Lee et al., Composites Sci. and Tech. **68**, 2485 - 2489 (2008).
13. Y. Gao et al., Ind. Eng. Chem. Res., **53**, 16777 - 16784 (2014).
14. O.-S. Kwon et al., Carbon, **58**, 116 - 127 (2013).
15. H.Ki Kim et al., Optics Express, **23**, 5900 (2015).
16. Rathmell A.et al, Adv. Mat., **23**, 4798 - 4803 (2011).
17. R.P. Tortorich and J.-W. Choi, Nanomaterials, **3**, 453 - 468 (2013).
18. K.-Y. Shin et al., Adv. Mater., **23**, 2113 - 2118 (2011).
19. S. K. Eshkalaka et al., Applied Materials Today, **9**, 372 - 386 (2017).
20. Y. Gao et.al., Ind. Eng. Chem. Res., **53**, 16777 16784 (2014).
21. J. Li et al., Adv. Mater.,**25**, 3985 - 399 (2013).
22. E. B. Secor et al., J. Phys. Chem. Lett., **4**, 1347 - 1351 (2013).
23. F. Mederos-Henry et al., J. Mater. Chem. C, **3**, 3290 (2016)
24. D. Ferreira et al., IEEE Trans. Antennas Propag., **63**, 3947 - 3955 (2015).
25. A. E. Yilmaz, M. Kuzuoglou, Radio Engineering, **18**, 95-102 (2009).
26. N. Quiévy et al., IEEE Trans. Electromag. Compatibility, **54**, 43-51 (2012).
27. Y. Gao et al., Ind. Eng. Chem. Res., 2014, 53 (43), pp 1677716784.
28. W. Baaziz et al., J. Phys. Chem. C, **118**, 37953810 (2014).
29. H. Lv, J. Mater. Chem. C, **3**, 10232 (2015).
30. W.W Lu et al., ACS Appl. Mater. Interfaces, **7**, 1940819415 (2015).
31. Z. Mo, Carbon, **144**, 433-439 (2019).
32. Q. Zhou et al., Materials and Design, **123**, 46-53 (2017).
33. H. Huang et al., ACS Appl. Mater. Interfaces, **10**, 4473144740 (2018).
34. Y. Zhang et. al., J. Mater. Chem., **21**, 14563-14568 (2011).